Received: 18 September 2022 | Revised: 9 December 2022 | Accepted: 7 January 2023

DOI: 10.1002/sus2.113

RESEARCH ARTICLE

SusMat WILEY

Enabling intercalation-type $TiNb_{24}O_{62}$ anode for sodium- and potassium-ion batteries via a synergetic strategy of oxygen vacancy and carbon incorporation

Ajay Piriya Vijaya Kumar Saroja[1] | **Zhipeng Wang**[2] | **Henry R. Tinker**[1] | **Feng Ryan Wang**[2] | **Paul R. Shearing**[3] | **Yang Xu**[1]

[1]Department of Chemistry, University College London, London, UK

[2]Materials and Catalysis Laboratory, Department of Chemical Engineering, University College London, London, UK

[3]Electrochemical Innovation Lab, Department of Chemical Engineering, University College London, London, UK

Correspondence
Yang Xu, Department of Chemistry, University College London, London WC1H 0AJ, UK.
Email: y.xu.1@ucl.ac.uk

Funding information
Engineering and Physical Sciences Research Council, Grant/Award Numbers: EP/V000152/1, EP/X000087/1; Leverhulme Trust, Grant/Award Number: RPG-2021-138; Royal Society, Grant/Award Numbers: RGS\R2\212324, SIF\R2\212002

Abstract

The key to develop earth-abundant energy storage technologies sodium- and potassium-ion batteries (SIBs and PIBs) is to identify low-cost electrode materials that allow fast and reversible Na^+/K^+ intercalation. Here, we report an intercalation-type material $TiNb_{24}O_{62}$ as a versatile anode for SIBs and PIBs, via a synergistic strategy of oxygen vacancy and carbon incorporation to enhance ion and electron diffusion. The $TiNb_{24}O_{62-x}$/reduced graphene oxide (rGO) composite anode delivers high reversible capacities (130 mA h g^{-1} for SIBs and 178 mA h g^{-1} for PIBs), great rate performance (54 mA h g^{-1} for SIBs and 37 mA h g^{-1} for PIBs at 1 A g^{-1}), and superior cycle stability (73.7% after 500 cycles for SIBs and 84% after 300 cycles for PIBs). The performance is among the best results of intercalation-type metal oxide anodes for SIBs and PIBs. The better performance of $TiNb_{24}O_{62-x}$/rGO in SIBs than PIBs is due to the better reaction kinetics of the former. Moreover, mechanistic study confirms that the redox activity of $Nb^{4+/5+}$ is responsible for the reversible intercalation of Na^+/K^+. Our results suggest that $TiNb_{24}O_{62-x}$/rGO is a promising anode for SIBs and PIBs and may stimulate further research on intercalation-type compounds as candidate anodes for large ion batteries.

KEYWORDS
anode, defects, intercalation, potassium-ion battery, sodium-ion battery, sustainability

1 | INTRODUCTION

Developing sustainable batteries have gained significant interest in recent years to accelerate the transition to net zero emission and tackle the issue of climate change.[1–6] Na- and K-ion batteries (SIBs and PIBs) are two promising candidates in this regard. However, the larger sizes of Na^+ (102 pm) and K^+ (138 pm) cause huge volume variation[2,7,8] and further lead to poor kinetics[9] in anode hosts, limiting the full utilization of the benefits in SIBs and PIBs. Although conversion and alloy-type anode materials have the merits of high specific capacity, balancing to

obtain both specific capacity and cyclability is still a great challenge due to huge volume expansion. For instance, the storage of K^+ in alloy-type anodes such as Sb exhibits a massive volume expansion of 407%.[10] In this regard, intercalation-type anodes have attracted rapidly growing attention because of the balance between specific capacity and durability along with low operating voltage. Exploring new intercalation-type anodes with minimal volume strain is highly desirable for the storage of large Na^+ and K^+. In recent years, intercalation-type metal oxides have gained much interest as low-strain anodes that work at a safe operating voltage compared to carbon-based intercalation anodes.[11–17]

Owning to low volume expansion and safe operating voltage, titanium niobium oxides belonging to the family of the Wadsley–Roth (WR) crystal structures have a great feature of the wide channels for ion diffusion in the structures. These materials possess block structures comprising of corner and edge sharing NbO_6 and TiO_6 octahedra units, forming open tunnel gaps perpendicular to the plane of the blocks and providing active site for Na^+/K^+ accommodation. The blocks are interconnected to form a shear plane by edge sharing octahedra and tetrahedra units (Figure 1A).[18,19] Due to these features, titanium niobium oxides have been demonstrated to be high-rate and low volume expansion (6%–17%) anode materials for Li-ion battery.[19–24] Considering the benefits of tunnel structure and the three-electron redox process of Ti^{4+} to Ti^{3+} and Nb^{5+} to Nb^{3+}, titanium niobium oxides could be considered potential anode materials for SIBs and PIBs, but unfortunately only one titanium niobium oxide, $TiNb_2O_7$, has been reported for SIBs so far. Huang et al. investigated the Na^+ storage performance of the amorphous $TiNb_2O_7$ phase synthesized by ball milling.[25] Although the amorphous $TiNb_2O_7$ delivered a good capacity of 180 mA h g^{-1} at a low current density of 15 mA g^{-1}, the rate performance was limited to 40 mA g^{-1} at 1 A g^{-1}, due to the poor conductivity of $TiNb_2O_7$. Focusing on rate performance, Cao's group introduced graphene to form a composite with $TiNb_2O_7$.[26] The $TiNb_2O_7$/graphene composite showed improved rate performance, but its cyclability was tested only for 70 cycles. Shang et al. also implemented a similar strategy by introducing multiwalled carbon nanotubes (CNTs) to $TiNb_2O_7$ to obtain a $TiNb_2O_7$/CNT composite.[27] It delivered a great capacity of 320 mA h g^{-1} at 50 mA g^{-1}, but the high loading of carbon (43.28%) may not favor the practical use of the composite. Despite the limited improvement in the SIB performance of $TiNb_2O_7$, to the best of our knowledge, there has been no report on the PIB performance of titanium niobium oxides. This directs our interest toward investigating titanium niobium oxides as versatile intercalation anodes for both SIBs and PIBs.

$TiNb_{24}O_{62}$ has a larger block size than $TiNb_2O_7$ and is further different from $TiNb_2O_7$ in a way that the tetrahedra TiO_4 units in the structure of $TiNb_{24}O_{62}$ connect the blocks, providing structural stability during the intercalation of large ions. However, there are shortcomings when these ions diffuse through the tunnels. The first and foremost factor is the energy barrier of Na^+/K^+ diffusion is much higher than that of Li^+. The energy barrier arises due to the occupancy of Na^+/K^+ in a 12-cordinate site in the center of the tunnels, which increases the repulsion of ions in the tunnels. This limits the ionic conductivity of Na^+/K^+ in $TiNb_{24}O_{62}$, which is correlated to energy barrier.[28] The second factor is the poor electrical conductivity ($<10^{-9}$ S cm^{-1}) of titanium niobium oxides,[29] which, combining with the ion diffusion energy barrier issue, further prevents the materials from realizing their structural benefits. Therefore, it is important to take on synergetic strategies to overcome both shortcomings and achieve favorable Na^+/K^+ storage in $TiNb_{24}O_{62}$.

In this work, we report for the first time $TiNb_{24}O_{62}$ (TNO) as a versatile intercalation-type anode for SIBs and PIBs through simultaneously incorporating oxygen vacancy (OV) and reduced graphene oxide (rGO) with $TiNb_{24}O_{62}$ via a single step. The obtained composite consisting of OV-containing TNO and rGO (TNO_x/rGO) exhibited reversible capacities of 130 mA h g^{-1} for SIBs and 178 mA h g^{-1} for PIBs at 20 mA g^{-1}, great rate capability at 1 A g^{-1}, and long-term cycling stability over 300–500 cycles. Our mechanistic study demonstrates the reversible intercalation of Na^+ and K^+ in TNO_x, and the obtained rate performance is attributed to the enhanced ion intercalation due to the presence of OVs and rGO, being different from the capacitive contribution from surface storage that is commonly seen from anode materials. We hope this work could provide experimental insights into the Na^+ and K^+ storage in the WR crystal structure and may spark further research interest on exploring other types of WR crystal structures for various beyond lithium energy storage technologies, where ions with large and high charge densities act as charge carriers.

2 | RESULTS AND DISCUSSION

An interconnected porous TNO was prepared by the sol–gel method, which is illustrated in Figure 1B. Compared with the solvothermal method widely used for the synthesis of titanium niobium oxides,[20,27,29–36] sol–gel method is scalable and hence implemented in this study. The synthesis method involves the hydrolysis and condensation of $C_{12}H_{28}O_4Ti$ and $Nb(OC_2H_5)_5$ in an acidic medium to form a gel. The heat treatment of the gel at 850°C yields

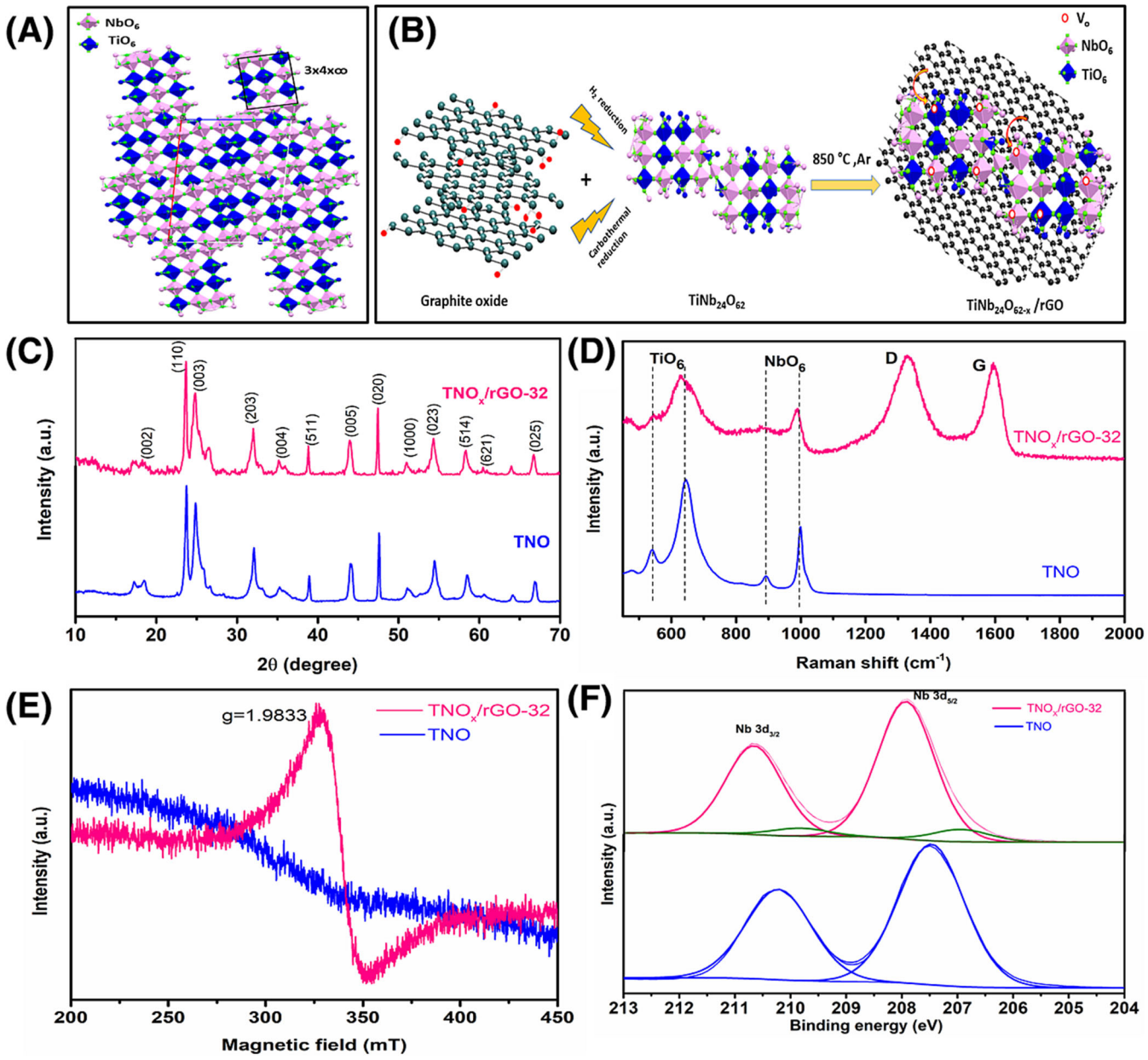

FIGURE 1 Schematic illustrations of the crystal structure of TNO (A) and the synthesis process of TNO_x/rGO (B). X-ray diffraction (XRD) patterns (C), Raman spectra (D), EPR spectra (E), and Nb 3d X-ray photoelectron spectrometer (XPS) spectra (F) of TNO and TNO_x/rGO-32.

porous TNO. The formation of the porous structure is due to the presence of acetic acid that acts as a pore forming agent. Acetic acid decomposes and generates CO_2 and H_2O at 440°C during the heat treatment,[37] which results in the generation of pores in TNO (Figure S1a,b). Simultaneous OVs and carbon incorporation in TNO are obtained in a single step of annealing the sol–gel-derived TNO and GO mixture in H_2 due to the simultaneous H_2 reduction of TNO to TNO_x and GO to rGO. The synergy here is that the oxygen functional groups on the surface of GO, such as carboxyl and epoxy, provide an anchoring support for TNO, and at the same time GO assists in introducing OVs via carbothermal reduction. The crystallinity and phase formation of TNO and TNO_x/rGO were confirmed by X-ray diffraction (XRD) (Figure 1C). The diffraction patterns are consistent with the monoclinic phase of $TiNb_{24}O_{62}$ as reported from the previous literature with no impure phases such as Nb_2O_5 and other titanium niobium oxides.[22,38–40] The wrapping of rGO over TNO_x does not alter the crystal structure of $TiNb_{24}O_{62}$ and the additional peak positioned at 26.5° in TNO_x/rGO corresponds to the (0 0 2) graphitic plane of rGO.[41,42] The

structure of TNO was also confirmed by Raman spectra (Figure 1D). The peaks at 541 and 644 cm^{-1} correspond to corner-shared and edge-shared TiO_6 octahedra, respectively. Corner- and edge-shared NbO_6 octahedra give rise to the peaks at 891 and 998 cm^{-1}, respectively.[20,22,29] These peaks also appear in TNO_x/rGO, which implies that the creation of OVs in TNO_x/rGO does not disrupt the structure of TNO. Along with the peaks of TiO_6 and NbO_6 octahedral units, TNO_x/rGO shows two peaks at 1328 and 1596 cm^{-1} corresponding to the D and G bands of rGO, respectively. The G band corresponds to the in-plane vibration of sp^2 carbons arising from C–C bond stretching, and the D band arises due to the presence of defects caused by graphite edges.[43,44] The wrapping of rGO also causes red shift of the peaks corresponding to TiO_6 and NbO_6 octahedra units, because the creation of OVs causes electron transfer between TNO and oxygen functional groups.[45] The formation of OVs in TNO_x/rGO is confirmed from the EPR measurements. TNO shows a flat line with no prominent EPR signal (Figure 1E), indicating that Ti and Nb are in the highest oxidation state and there are no free electrons in pristine TNO. TNO_x/rGO shows a strong signal at a *g*-value close to 1.98, which confirms the presence of OVs.[30,46] As a result, the oxidation states of Nb and Ti reduce, which introduces free electrons for charge compensation, thereby generating EPR signal. Furthermore, the high resolution Nb 3d X-ray photoelectron spectrometer (XPS) spectrum of TNO (Figure 1F) shows two distinct peaks at 210.2 and 207.4 eV, corresponding to Nb^{5+} $3d_{3/2}$ and Nb $3d_{5/2}$, respectively.[22] For TNO_x/rGO, a set of peaks at lower binding energies of 209.8 (Nb $3d_{3/2}$) and 206.9 eV (Nb $3d_{5/2}$) confirms the partial reduction of Nb^{5+} to Nb^{4+}. The creation of OVs causes charge redistribution in TNO leading to the lowered oxidation state of the metal ions.[30,47,48] As OVs are induced by the synergistic roles of hydrogen treatment and carbothermal reduction, mixtures with different TNO:GO ratios (2:1, 1:1, and 1:2) were subjected to the same treatment, which resulted in the rGO contents of 18, 32, and 48 wt%, respectively (denoted as TNO_x/rGO-18, TNO_x/rGO-32, TNO_x/rGO-48), in the final TNO/rGO composites (Figure S2, TNO_x/rGO-32 is chosen as the representative anode in our discussions). Initially, TNO without any GO was subjected to hydrogen reduction treatment, which also created OVs in TNO (i.e., TNO_x) with an Nb^{4+} content of 4.4% (Table S1). As expected, the content of Nb^{4+} increased to 5.1%, 5.8%, and 6.3% in TNO_x/rGO-18, TNO_x/rGO-32, and TNO_x/rGO-48, respectively (Figure S3 and Table S1). This confirms the synergistic strategy that carbothermal reduction induced by oxygen functional groups in GO assists in the formation of OVs in TNO alongside with the hydrogen reduction of TNO. Using this strategy, OV content can be controlled without altering synthesis conditions.

The morphology of TNO represents interconnected particles with pores between the particles (Figure 2A). The enlarged scanning electron microscope (SEM) image highlights the presence of interconnected pores that distribute throughout the sample. To confirm the nature of the porosity in TNO and TNO_x/rGO-32, pore size distribution was measured from N_2 adsorption desorption isotherm. The isotherm represents type IV isotherm that is an indication of mesoporous materials (Figure S4a). The surface area of TNO and TNO_x/rGO-32 is 4.5 and 16.7 m^2 g^{-1}, respectively. The increase in surface area of TNO_x/rGO-32 is due to the incorporation of rGO. The pore size distribution of TNO and TNO_x/rGO-32 centers at 3.8 and 3.4 nm (Figure S4b), respectively, signifying the presence of mesopores. The presence of the pores assists in electrolyte penetration and ion transfer. The wrapping of rGO on TNO_x resulted in anchoring of TNO_x particles on rGO surface without significant agglomeration compared to prsitine TNO (Figure 2B). The distribution of TNO_x on rGO prevents particle aggregation during the insertion and extraction of Na^+/K^+. A transmission electron microscope (TEM) image further reveals the microstructure and crystallinity of TNO_x (Figure 2C,D). The thin layers of rGO cover the surface of TNO_x, which is beneficial for the fast charge transfer between TNO_x and rGO. An HRTEM image of TNO_x/rGO-32 (Figure 2D) demonstrates the high crystallinity of TNO_x with a d-spacing of 0.331 nm corresponding to the (1 1 3) plane of TNO. Moreover, EDS mapping of TNO_x/rGO shows the presence of Ti, Nb, O, and C, confirming the distribution of TNO_x on the rGO sheets (Figure 2E–I).

To demonstrate the benefit of OVs and carbon matrix for storing large ions in TNO_x, a series of samples, including TNO, TNO_x/rGO-18, TNO_x/rGO-32, and TNO_x/rGO-48, were tested. Initially, the Na^+ storage behavior of TNO and TNO_x/rGO-32 was investigated using cyclic voltammetry (CV) in the potential range of 0.01 to 3 V at the scan rate of 0.05 mV s^{-1} (Figure 3A,B). In the first cycle, a broad and irreversible cathodic current is observed due to the formation of solid-electrolyte interphase (SEI) layer and the irreversible trapping of Na^+ within the TNO structure. In the further cycles, CV curves overlap with each other reflecting the reversibility of the reaction. The redox couple appearing in the broad potential range of 0.8 to 1.25 V in TNO and TNO_x/rGO-32 corresponds to the change in valence state of Ti^{4+}/Ti^{3+}.[49,50] The redox pair that appears at 0.47 and 0.46 V in TNO_x/rGO-32 corresponds to the redox reaction of Nb^{5+}/Nb^{4+}.[51–53] It is worth noting that the intensity of these redox peaks is more prominent in TNO_x/rGO-32 due to enhanced intercalation and reversibility compared to TNO, in contrast to the broad redox peaks appearing in a wide potential range in TNO, which highlights that the charge storage process

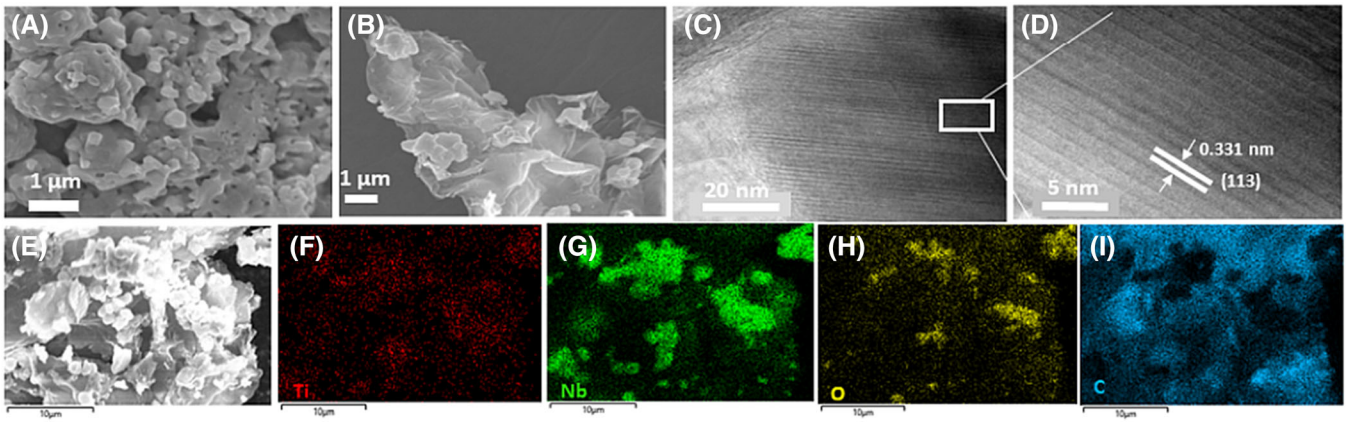

FIGURE 2 Scanning electron microscope (SEM) images of TNO (A) and TNO_x/rGO-32 (B). HR transmission electron microscopy (HRTEM) images (C and D) and EDX mapping (E–I) of TNO_x/rGO-32.

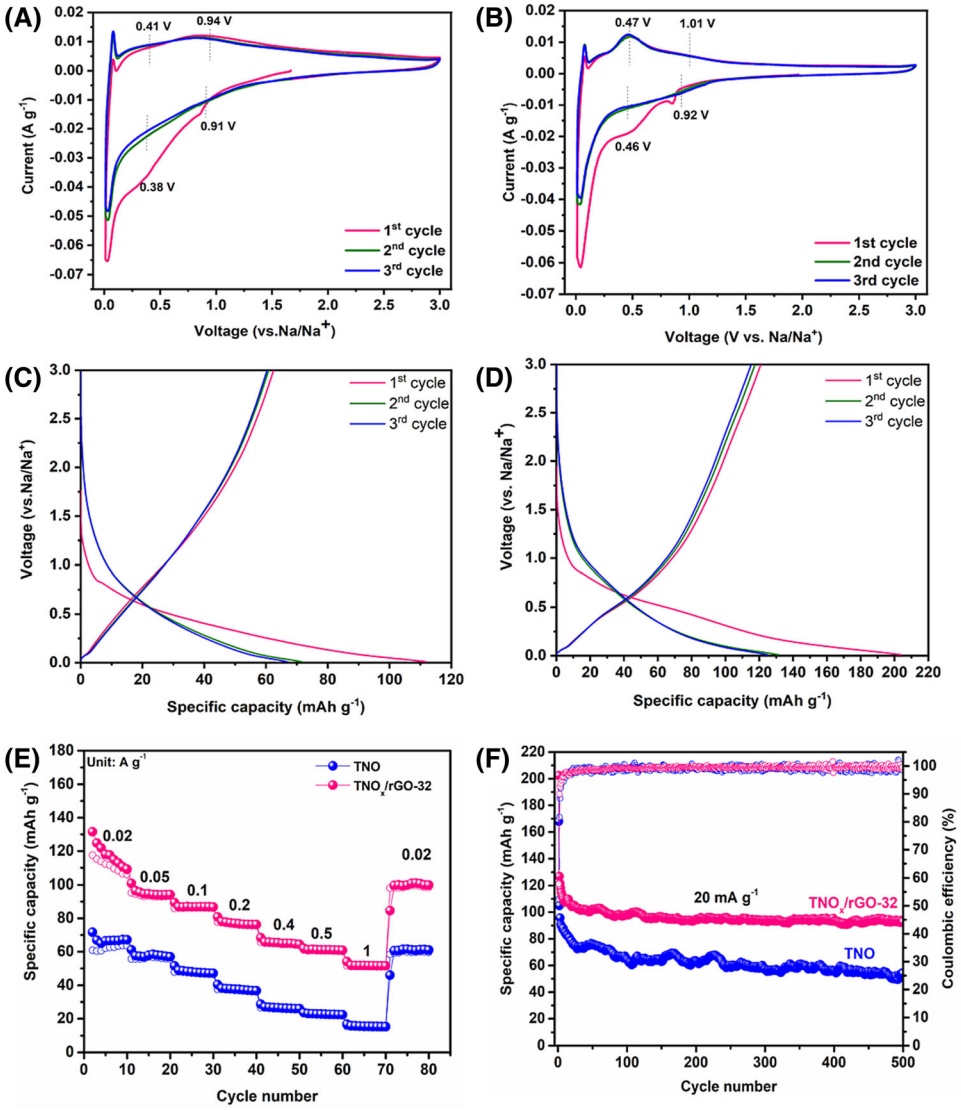

FIGURE 3 Cyclic voltammetry (CV) curves of TNO (A) and TNO_x/rGO-32 (B) in Na cells in the range of 0.01–3 V and a scan rate of 0.05 mV s^{-1}. GCD profiles of TNO (C) and TNO_x/rGO-32 (D) in the first three cycles of Na cells at 20 mA g^{-1}. Comparison of rate capability (E) and cycle stability (F) of TNO and TNO_x/rGO-32 in Na cells.

in TNO occurs mainly by pseudocapacitance rather than intercalation. An anodic peak that appears around 0.07 V is due to the interaction of Na^+ in super P (conductive additive in the electrode, Figure S5). In consistent with the CV curves, there are no distinct voltage plateaus in the GCD profiles of TNO (Figure 3C). The sloping-shaped profiles indicate that an intercalation of Na^+ into the tunnels of TNO occurs via Faradaic charge transfer with no phase transformation.[54–56] TNO delivers a reversible discharge capacity of 71 mA h g^{-1} at the current density of 20 mA g^{-1}, and the creation of OVs and rGO wrapping in TNO_x/rGO-32 significantly increases the capacity to 130 mA h g^{-1} (Figure 3D). Moreover, the storage of Na^+ in TNO_x/rGO-32 is more reversible compared to TNO, which is evident from initial coulombic efficiency (ICE). The ICE of TNO_x/rGO-32 is 59% that is higher than that of TNO (55%), further illustrating the reversibility of the reaction in TNO_x/rGO-32. The presence of a conductive network and OVs improves the electrical conductivity of the anode and facilitates the diffusion of Na^+ within TNO_x, thereby lowering diffusion barrier and promoting reversible intercalation and deintercalation processes. This overrides the irreversible capacity loss that occurred during the SEI layer formation in TNO_x/rGO-32. At a high current density of 1000 mA g^{-1}, TNO_x/rGO-32 delivers a specific capacity of 54 mA h g^{-1} that is ~3 times higher than that of TNO (Figure 3E). Rate performance of TNO_x without rGO, TNO_x/rGO-18, TNO_x/rGO-48 was also evaluated (Figure S6). TNO_x delivers a much higher capacity of 36 mA h g^{-1} than TNO at 1000 mA g^{-1}. With 18 wt% rGO, the specific capacity slightly increases to 41 mA h g^{-1} and further increasing rGO content to 48% increases the capacity to 73 mA h g^{-1} at 1000 mA g^{-1}, which is better than the previously reported rate capability of $TiNb_2O_7$.[25] Obviously, the combined benefit of OVs and rGO wrapping contributes to fast electron transfer and Na^+ diffusion transport at the high current density. Additionally, long-term cyclability of TNO and TNO_x/rGO-32 at 20 mA g^{-1} was shown in Figure 3F. TNO exhibits rapid capacity fading and shows a capacity retention of 51.2% after 500 cycles, with low CEs in the initial few cycles (81.6%, 88.4%, and >90% at the 2nd, 3rd, and 40th cycles, respectively). In the case of TNO_x/rGO-32, the CE stabilizes at 98% after 20 cycles, and as a result the cyclability of TNO_x/rGO-32 significantly improved with the capacity retention of 73.7% after 500 cycles (Figure 3F). Compared with previous reports on titanium niobium oxide anodes for SIBs (54.5% capacity retention after 500 cycles with the presence of 43.3% CNTs[27] and cyclability up to 70 cycles with the presence of 40% graphene[26]), TNO_x/rGO-32 exhibits better cyclability with good capacity retention. The existence of OVs prevents the repulsion of Na^+ with the cations in the TNO_x structure, enabling a great structural stability of TNO_x, and the presence of rGO provides fast electron transfer and keeps the composite's structure intact during cycles.

The electrochemical K^+ storage performances of TNO and TNO_x/rGO-32 were also evaluated in the potential range of 0.01 to 3 V (vs. K/K^+). CV measurements were carried out at the scan rate of 0.05 mV s^{-1} for three cycles (Figure 4A,B). The reduction peaks of TNO_x/rGO-32 appearing at 0.58 and 0.92 V in the first cycle correspond to SEI layer formation. The redox pair of 0.9 V/0.8 V corresponds to the change in the oxidation state of Ti. The oxidation peak at 0.6 V and a broad reduction peak in the range of 0.76–0.41 V centering at 0.53 V corresponds to the change in the oxidation state of Nb^{5+}/Nb^{3+}. Moreover, there is a prominent difference between the CV curves of TNO and TNO_x/rGO-32, where CV curves of TNO represent more of pseudocapacitive nature compared to TNO_x/rGO-32. Also, the peak currents of TNO_x/rGO-32 are higher, indicating that the intercalation/deintercalation of K^+ is facilitated compared to TNO. While comparing the CV curves of TNO and TNO_x/rGO-32 in SIBs and PIBs (Figures 3A and 4A), there is a difference in the peak position. The anodic peaks of TNO in PIBs are at 0.16 V higher voltage than in SIBs, close to the difference in the standard reduction potentials (~0.2 V) between K^+/K and Na^+/Na. The difference in anodic peak positions of TNO_x/rGO-32 is observed to be slightly less than 0.16 V due to the incorporation of rGO. The reversibility of K^+ intercalation in TNO_x/rGO-32 is also evident from the higher ICE of 55% in comparison to 50.8% for TNO. Similar to the GCD profiles for Na^+ storage, TNO and TNO_x/rGO for K^+ storage show a semi-linear GCD profile without defined intercalation voltage plateaus (Figure 4C,D). This signifies that K^+ storage in TNO also occurs by pseudocapacitance with no phase transformation. As shown in Figure 4E, at a low current density of 20 mA g^{-1}, TNO_x/rGO-32 delivers a reversible specific capacity of 178 mA h g^{-1}, being 3.2 times higher than that of TNO, and outperforms previously reported intercalation-type metal oxide (Ti-based) anodes for PIBs.[57–59] As the current density increased to 50, 100, 200, 400, and 500 mA g^{-1}, the specific capacities were 116, 91, 76, 57, and 49 mA h g^{-1}, respectively. Even at 1 A g^{-1}, a capacity of 37 mA h g^{-1} was obtained, completely outperforming TNO (<10 mA h g^{-1}). This signifies that TNO_x/rGO-32 provides more active sites for K^+ storage and can be a promising PIBs anode. To better understand the capacity contribution of rGO in TNO_x/rGO, the electrochemical performance of pristine rGO was tested at various current densities (Figure S7). The pristine rGO delivered reversible capacities of 101 and 156 mA h g^{-1} at 20 mA g^{-1} for SIBs and PIBs, respectively. Taking consideration of the TNO_x/rGO weight ratio of 68/32 in TNO_x/rGO-32, rGO can contribute ~1/3 of the overall capacity, being 44 and 60 mA h g^{-1} in

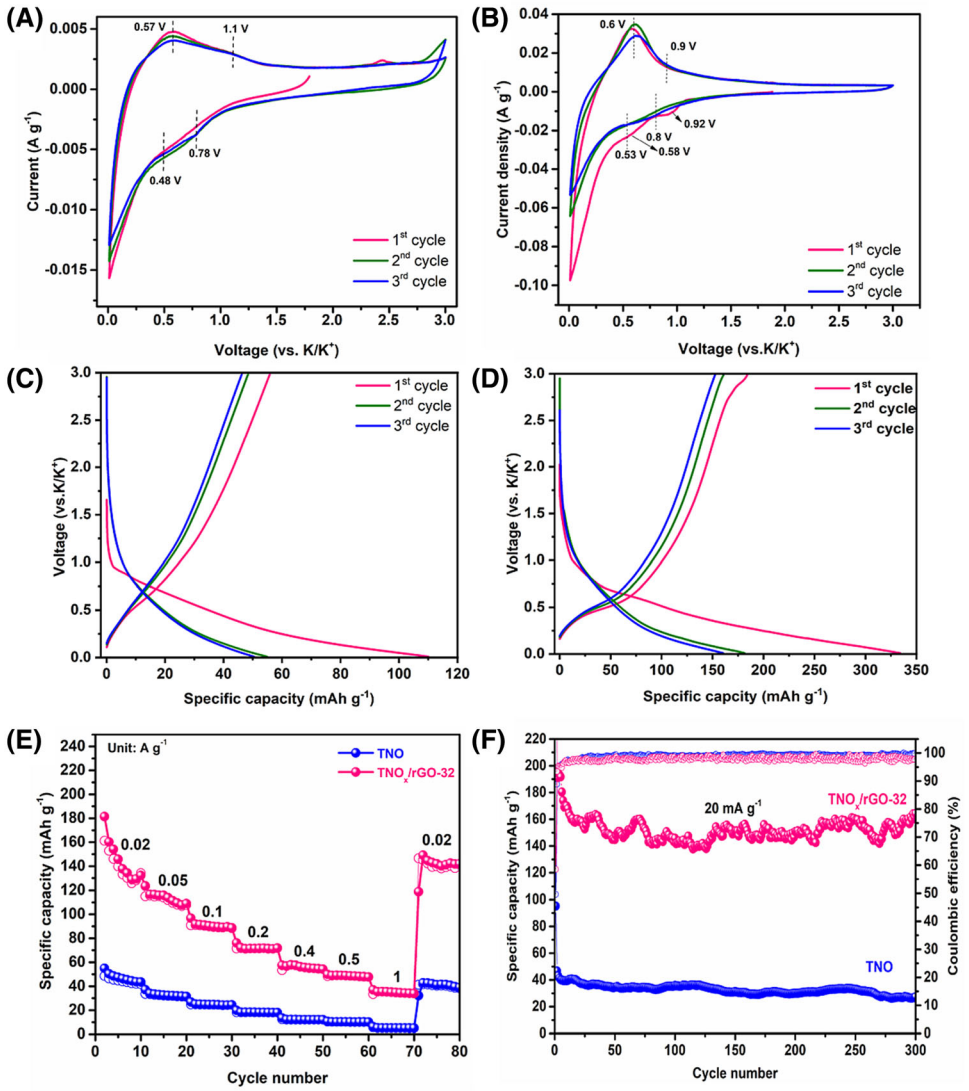

FIGURE 4 Cyclic voltammetry (CV) curves of TNO (A) and TNO_x/rGO-32 (B) in K cells at the range of 0.01–3 V and the scan rate of 0.05 mV s^{-1}. GCD profiles of TNO (C) and TNO_x/rGO-32 (D) in the first three cycles of K cells at 20 mA g^{-1}. Comparison of rate capability (E) and cycle stability (F) of TNO and TNO_x/rGO-32 in K cells.

SIBs (131 mA h g^{-1}) and PIBs (181 mA g^{-1}), respectively. Therefore, the capacity in TNO_x/rGO is mainly contributed from TNO due to the enhanced reaction kinetics, benefiting from the synergistic role of OV and rGO. Looking at the different contents of rGO and OVs (Figure S8), the presence of a low carbon content of 18% does not greatly improve the performance (~13 mA h g^{-1} at 1000 mA g^{-1}), whereas increasing the rGO content to 48 wt% improved the capacity to 46 mA h g^{-1}. When cycled at 20 mA g^{-1}, TNO_x/rGO-32 retains 84% capacity, delivering 164 mA h g^{-1} after 300 cycles (Figure 4F), whereas TNO exhibits rapid capacity fading with only 55% capacity retention after 300 cycles. The long-term cycling stability of TNO_x/rGO-32 is once again much higher than the reported Ti-based intercalation anodes for PIBs, such as $K_2Ti_4O_9$ (56% capacity retention after 30 cycles at 100 mA g^{-1}),[60] $K_2Ti_8O_{17}$ (62% after 50 cycles at 20 mA g^{-1}),[61] and carbon-coated $KTi_2(PO_4)_3$ (55.5% after 50 cycles at 20 mA g^{-1}).[62] The comparison here demonstrates the reversibility and structural stability of TNO_x/rGO-32, which is enabled by the OVs and carbon incorporation collectively.

Na^+/K^+ storage mechanism of TNO_x/rGO-32 was investigated by the XRD and XPS measurements of the electrodes after initial discharge and charge processes. Figure 5A shows the Nb 3d XPS spectra (Ti signal was too weak to be detected, presumably due to the very low Ti content in the composite). Pristine TNO_x/rGO-32 electrode shows the existence of Nb^{5+} as confirmed from the peak positions at 207.6 and 210.3 eV. The coexistence of Nb^{4+} is due to the partial reduction of Nb^{5+} caused by OVs. After the first discharge process in the Na cell, the Nb^{5+} peaks are weakened, whereas the Nb^{4+} peaks at 209.3

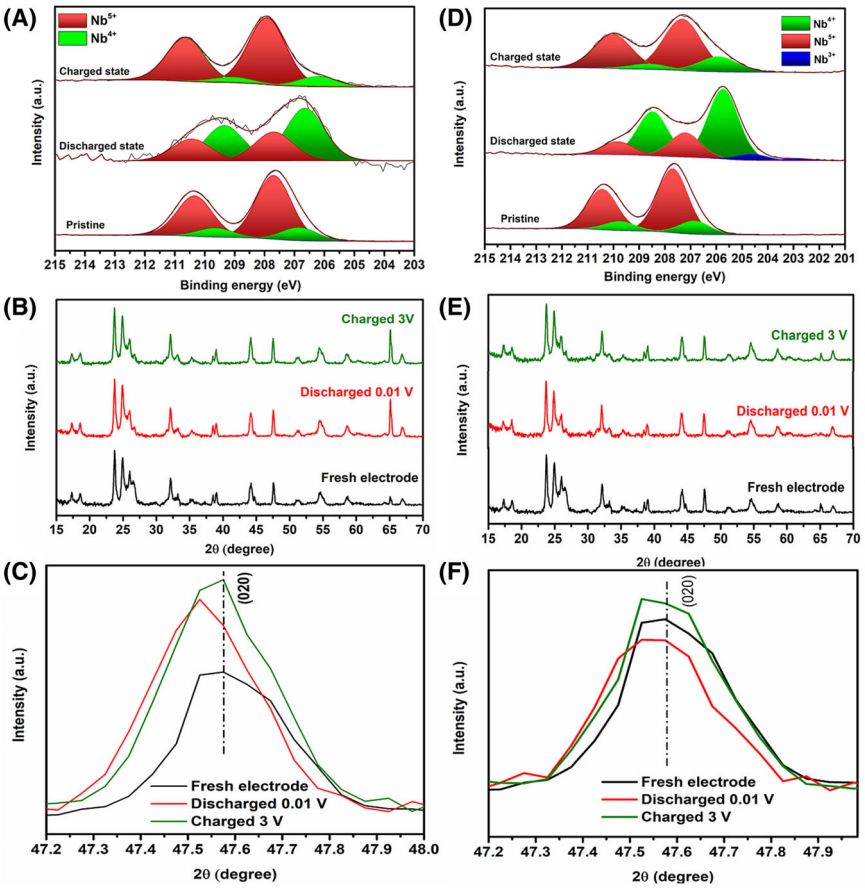

FIGURE 5 Nb 3d X-ray photoelectron spectrometer (XPS) spectra (A and D), X-ray diffraction (XRD) patterns (B and E), and enlarged (0 2 0) peak (C and F) of TNO_x/rG-32 at pristine, discharged, and charged states in Na cells (A–C) and K cells (D–F).

and 206.6 eV are intensified, which confirms the intercalation of Na^+ causes the reduction of Nb. In the following charged state, the intensity of the Nb^{5+} peaks resumed to the pristine state along with weak Nb^{4+} peaks. This confirms Na^+ can be intercalated and deintercalated into the TNO_x/rGO-32 structure reversibly. Likewise, the intercalation of K^+ causes the change in the oxidation state of Nb with an increased intensity of Nb^{4+} (Figure 5D). In addition, there are noticeable reductions of Nb^{4+} to Nb^{3+}, which could be responsible for the higher specific capacity for PIBs compared to SIBs. In the subsequent charged state, Nb^{3+} and Nb^{4+} are oxidized back to Nb^{5+} with the presence of a small amount of Nb^{4+}, due to the presence of OVs. These results clearly depict the reversible K^+ intercalation in TNO_x/rGO-32. The structural stability of TNO_x/rGO-32 at charged and discharged states was verified by XRD. As seen from Figure 5B, the XRD patterns are almost identical and no new peaks can be identified. Intercalation of Na^+ causes a slight downward shift of the (0 2 0) diffraction peak at 47.6° (Figure 5C). The diffusion of Na^+ along the *b*-axis causes an expansion leading to the (0 2 0) peak shift. In the charged state, the peak shifts back to the original position, indicating the reversibility of Na^+ (de)insertion. Intercalation of K^+ also causes the shift of the (0 2 0) peak toward a lower angle at the discharged state and resumes back to the original position at the charged state (Figure 3E,F). To understand the structural stability of TNO_x/rGO, the surface morphology of cycled electrodes was observed from SEM images (Figure S9). TNO_x/rGO electrode before cycling shows the homogeneous distribution of active material, binder and super P (Figure S9a). After cycling, the electrode retained the surface morphology without forming any cracks in SIBs (Figure S9b). Also, there is no variation in the particle size of TNO_x compared to its pristine state, indicating the structural stability of the electrode. Cycled electrode in PIBs shows rGO sheets being oriented vertically on the surface of the electrode (Figure S9c), suggesting a structural rearrangement to some extent. Nevertheless, TNO_x particles kept intact with rGO and no cracks were observed. rGO standing between clusters of particles might act as a reinforcement layer to provide structural stability to the electrode without losing the improvement in electronic conductivity.[63]

To differentiate the capacity contribution of diffusion- and surface-controlled processes in TNO and TNO_x/rGO-32, CV curves at different scan rates were recorded in the potential range of 0.01 to 3 V (Figure S10). As the scan rate (ν) increases, the peak currents (i) of both TNO and TNO_x/rGO-32 increase. According to the general expression of $i = a\nu^b$, where a and b are adjustable constants,

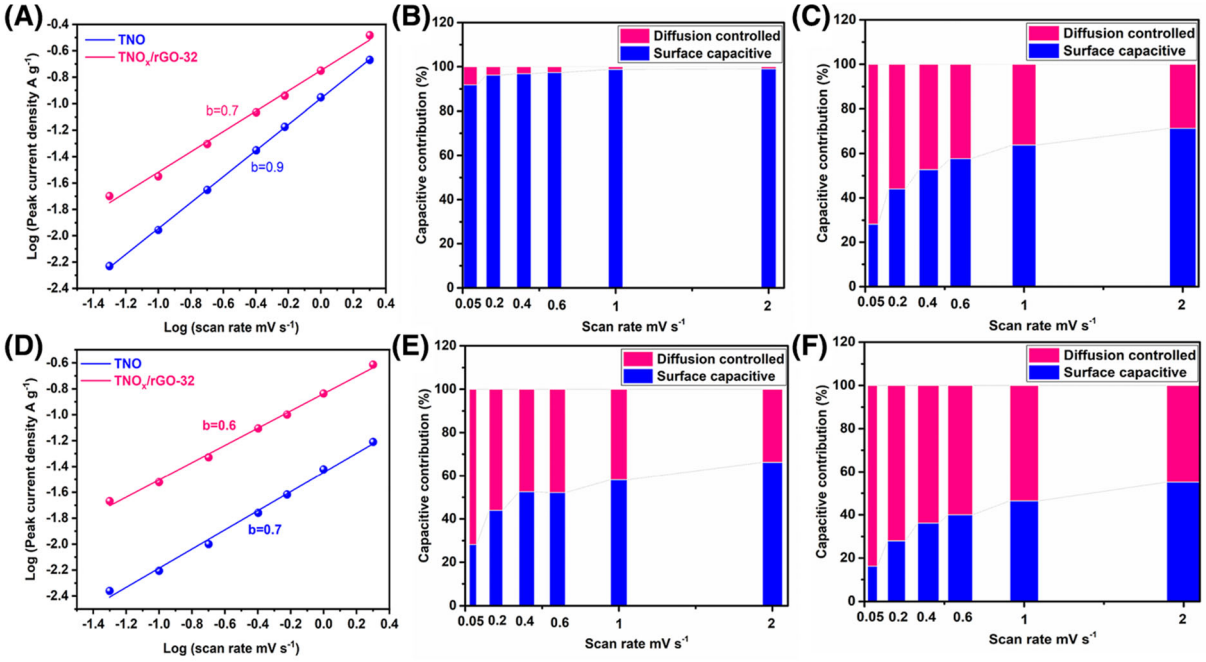

FIGURE 6 Logarithmic relationship between scan rate and anodic peak current of TNO and TNO_x/rGO-32 in Na cells (A) and K cells (D). Capacity contributions at various scan rates of TNO (B and E) and TNO_x/rGO-32 (C and F) in Na cells (B and C) and K cells (E and F).

the *b*-value would be 0.5 for an ideal semi-infinite linear diffusion controlled process while close to 1.0 for a surface-controlled capacitive process.[64,65] The plots of log(*i*) versus log(*ν*) for the anodic peak current in the CV curves of TNO and TNO_x/rGO-32 for SIBs and PIBs are shown in parts (A) and (D) of Figure 6, respectively. In the case of SIBs, the *b*-value for TNO is 0.9, indicating that the charge storage process is largely controlled by surface capacitive process. However, the *b*-value of TNO_x/rGO-32 drops down to 0.7, and it suggests that despite the heavier reliance on diffusion-controlled process to storage ions, TNO_x/rGO-32 still delivered a better performance than TNO. This, in turn, demonstrates the improved Na^+ diffusion and intercalation in TNO_x/rGO-32, which is enabled by the simultaneous presence of OVs and rGO. The contribution of capacitive-controlled ($k_1\nu$) and diffusion-controlled ($k_2\nu^{1/2}$) processes can be calculated using $i(V) = k_1\nu + k_2\nu^{1/2}$, where *i* is the total current response at a fixed potential (*V*), k_1 and k_2 are constants at a particular scan rate. At the scan rate of 0.05 mV s^{-1} in the Na cells, the diffusion-controlled process contributes to about 72% to the overall capacity in TNO_x/rGO-32, whereas that of TNO is only ~8% (Figure 6B,C). At low scan rates, the presence of OVs facilitates the intercalation of Na^+ through the tunnels, which enhances a diffusion-controlled process for charge storage. Even at a high scan rate of 2 mV s^{-1}, TNO_x/rGO-32 has a lower *b*-value and less capacitive contribution compared to TNO, and yet TNO_x/rGO-32 exhibits a higher capacity. In the case of PIBs, TNO and TNO_x/rGO-32 show *b*-values of 0.7 and 0.6, respectively (Figure 6D). Once again, the latter is more limited to the diffusion-controlled process to store K^+ compared to the former, but the latter delivered higher capacities at all rates. The contributions of diffusion-controlled process in TNO_x/rGO-32 are 84% at 0.05 mV s^{-1} and 50% at 2 mV s^{-1}, whereas the values are 80% and 45% in TNO. Therefore, the results here clearly prove that the diffusion of Na^+ and K^+ is boosted by the synergistic benefits from rGO and OVs in TNO_x/rGO.

The galvanostatic intermittent titration technique (GITT) profiles for SIBs and PIBs are presented in Figure 7A,B, respectively, and the calculated D_{Na} and D_K are shown in Figure 7C,D, respectively (the method of *D* calculation is provided in Figure S8). The overpotential for TNO_x/rGO-32 is lower compared to TNO for both SIBs and PIBs (Figure 7A,B), reflecting better reaction kinetics. The higher average D_{Na} of TNO_x/rGO-32 (2.48×10^{-10} cm^2 s^{-1}) in comparison with TNO (0.84×10^{-10} cm^2 s^{-1}) implies that OVs greatly improve the diffusion and transport of Na^+. Similarly, K^+ diffusion in TNO_x/rGO-32 is greatly improved, as seen from the average D_K of TNO_x/rGO-32 being ~6.9 times higher than that of TNO (7.48×10^{-11} vs. 1.07×10^{-11} cm^2 s^{-1}). The overall trend of D_{Na} and D_K remains the same, with higher values at higher discharge voltages and lower values at lower discharge voltages (<0.4 V). This is because at the initial stage of the discharge process, a high concentration gradient of ions exists, as there are no ions available in the materials,

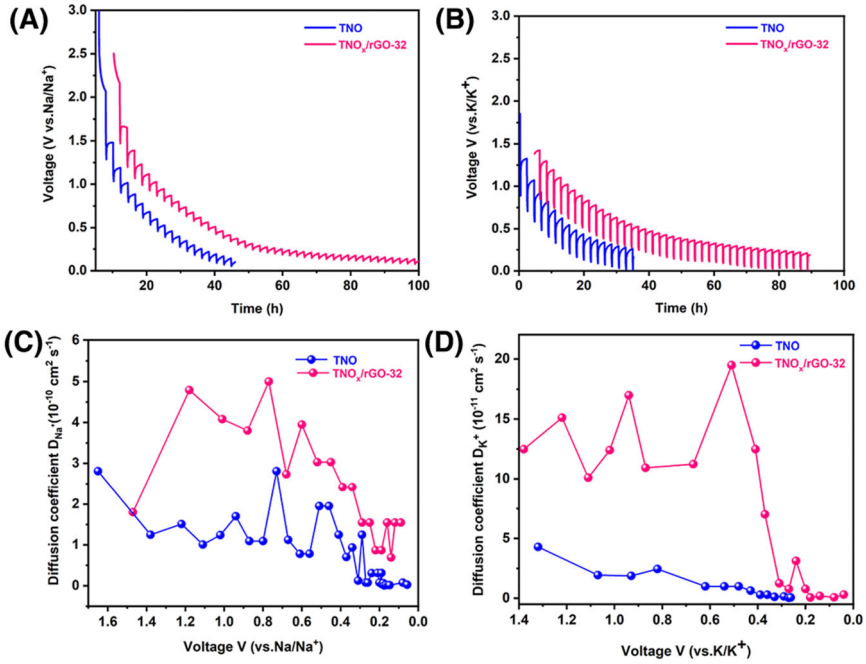

FIGURE 7 Transient voltage profiles of GITT (A and B) and comparison of diffusion coefficients during the discharge process (C and D) of TNO and TNO$_x$/rGO-32 in Na cells (A and C) and K cells (B and D).

whereas the concentration gradient decreases during the progress of discharge, resulting in the gradually decrease in ion concentration gradient, which decreases the facilitation of ion diffusion.[22,66,67] Moreover, D_{Na} and D_K are higher at 0.7 and 0.5 V, respectively, corresponding to the potentials at which Nb^{5+} being reduced to Nb^{4+}. Hence, it is apparent that TNO$_x$/rGO-32 has better reaction kinetics due to the improved Na^+/K^+ transport. Along with ion diffusion, the presence of rGO promotes electron transfer, which is another important contributing factor to the observed electrochemical performance. This is verified by the electrochemical impedance spectroscopy (EIS) results shown in Figure S12. TNO$_x$/rGO-32 has a charge transfer resistance (R_{ct}) of 23.1 Ω, being ~18 times lower than that of TNO. Therefore, the collective results of GITT and EIS demonstrate the enhancement of electron transfer and ion diffusion in TNO$_x$/rGO-32, leading to its versatility as an intercalation-type anode for both SIBs and PIBs.

3 | CONCLUSIONS

In summary, $TiNb_{24}O_{62-x}$/rGO were successfully prepared and demonstrated for the first time as a versatile anode for SIBs and PIBs. The anode exhibited high reversible capacities of 130 and 178 mA h g^{-1} for SIBs and PIBs, respectively. The composite structure can provide enhanced ion diffusion and a conductive carbon network, which results in great rate capability at 1 A g^{-1} and long-term cycling stability over 500 cycles for SIBs and 300 cycles for PIBs. The obtained electrochemical performance is among the best results of intercalation-type metal oxide anodes for PIBs. Furthermore, electrochemical kinetic study highlighted that diffusion-controlled ion storage was significantly enhanced by the synergistic strategy of introducing OV and carbon network. $TiNb_{24}O_{62-x}$/rGO showed better electrochemical performance in SIBs compared to PIBs, concluded from higher Na^+ diffusion coefficient and better rate capability, without significant sacrifice in durability. Our work showcases the promise of intercalation-type metal oxides in storing large ions without major structural change, and the method present in the work can also be extended to other functional oxide electrode materials for various sustainable energy storage technologies.

4 | EXPERIMENTAL SECTION

4.1 | Materials synthesis

4.1.1 | Synthesis of TNO

TNO was synthesized by the sol–gel method using niobium ethoxide ($Nb_2(OC_2H_5)_{10}$), titanium isopropoxide ($C_{12}H_{28}O_4Ti$), acetic acid (CH_3COOH), and ethanol (C_2H_5OH). Typically, 0.0596 g $C_{12}H_{28}O_4Ti$, 1.622 g ($Nb_2(OC_2H_5)_{10}$, and 1 ml CH_3COOH were added into 20 ml C_2H_5OH and the solution was stirred for 1 h. The solution then was dried at 60°C to remove the solvent and heated at 80°C for 12 h. The obtained product was annealed at 850°C for 4 h in a furnace at a heating rate of 5°C min^{-1} under an air atmosphere to obtain crystallized TNO.

4.1.2 | Synthesis of TNO_x/rGO

Graphite oxide (GO) was prepared using the Hummer method.[68] Graphite was oxidized using potassium permanganate ($KMnO_4$), with sodium nitrate ($NaNO_3$) present in sulfuric acid (H_2SO_4) in an ice bath. The mixture was then stirred for 1 h before 90 ml deionized (DI) water was added, followed by a continued stirring for 1 h. To make the mixture diluted, 292 ml DI water was added. Then, 12 ml hydrogen peroxide (H_2O_2, 30 wt%) was added to remove the unreacted $KMnO_4$ in the mixture. The mixture was centrifuged and washed several times until the pH was neutral. The obtained GO was dried at 60°C overnight in a vacuum oven. For the synthesis of TNO_x/rGO composite, different ratios of GO to TNO were mixed in 100 ml ethanol (C_2H_6O) and stirred for 24 h. The mixture was then dried to obtain dry powders. The final composite product was obtained by annealing the dry powders in a tubular furnace under N_2/H_2 (95/5%) gas at 800°C for 4 h.

4.2 | Materials characterization

XRD measurements were carried out using a STOE SEIFERT diffractometer with Mo X-ray source. The surface morphologies of TNO and TNO_x/rGO were characterized by a SEM (SEM, JEOL JSM 7600) and a TEM (TEM, JOEL-2100). The chemical states of different elements and oxidation state of Nb in TNO_x/rGO were evaluated by an XPS (XPS, Thermo Scientific *K*-alpha photoelectron spectroscopy) with Al *K*-alpha (1486.6 eV) as the X-ray source. Data analysis of XPS results was obtained using CasaXPS with the calibration of C 1s at 285 eV. The loading of rGO in TNO_x/rGO composites was obtained using a thermogravimetric analyzer (TGA, PerkinElmer STA6000.) in an air atmosphere with a heating rate of 10°C min^{-1}. Raman spectra were recorded with a Renishaw Raman spectrometer system using 633 nm laser. Electron paramagnetic resonance spectra were performed in a Bruker E580 X-band EPR spectrometer. EPR spectra (EPR, Bruker E580) were acquired with the sweep time 60 s, microwave frequency 9.45 GHz at room temperature. The nitrogen sorption isotherms were taken from the gas Sorption Surface Area and Pore Size Analyzer (Quantachrome, QUADRASORB evo). The materials were degassed in a vacuum at 180°C for 6 h. The Brunauer–Emmett–Teller method and Barrett–Joyner–Halenda model were used to calculate the specific surface area and pore size distribution, respectively.

4.3 | Electrochemical measurements

Electrochemical measurements were carried out using CR 2032-coin cells. For the fabrication of electrodes, active materials, super P, and sodium carboxylmethyl cellulose were homogeneously mixed in the mass ratio of 7.5:1.5:1 with DI water. The slurry was coated on a Cu foil and then dried at 70°C for 16 h under vacuum. Coin cells were assembled using TNO or TNO_x/rGO as the working electrode, sodium, or potassium metal as the counter and reference electrode in an argon-filled glove box (H_2O < 0.5 ppm, O_2 < 0.5 ppm). The electrolyte for SIBs was 1 M sodium perchlorate ($NaClO_4$) dissolved in a mixture of 1:1 volume ratio of ethylene carbonate and propylene carbonate (EC:PC), and the electrolyte for PIBs was 1 M potassium bis(fluorosulfonyl)imide (KFSI) dissolved in a mixture of 1:1 volume ratio of EC and PC. Glass fiber membrane (Whatman, GF-B) was used as the separator. Electrochemical measurements, including galvanostatic charge discharge (GCD), CV, EIS, and GITT, were carried out at room temperature. GCD and GITT measurements were carried out using Neware battery cyclers (BTS4000-5V10MA) in the potential range of 0.01–3 V at various current densities. CV and EIS measurements were carried out using Biologic potentiostat (VSP). CV was carried out in the potential range of 0.01–3 V at various scan rates. EIS was carried out in the frequency range of 1 MHz to 10 mHz with a voltage amplitude of 10 mV. For the ex situ characterization of the cycled electrodes, cells were disassembled inside a glove box and electrodes were washed with clean PC. They were then dried inside the glove box before the ex situ characterization. The electrodes were transferred to the characterizations in an airtight case to avoid the exposure to oxygen and moisture.

ACKNOWLEDGMENTS

Y.X. acknowledges the support of the Engineering and Physical Sciences Research Council (EP/V000152/1, EP/X000087/1), Leverhulme Trust (RPG-2021-138), and Royal Society (RGS\R2\212324, SIF\R2\212002). For the purpose of open access, the author has applied a Creative Commons Attribution (CC BY) license to any author-accepted manuscript version arising.

CONFLICT OF INTEREST STATEMENT

The authors declare no conflict of interest.

ORCID

Yang Xu https://orcid.org/0000-0003-0177-6348

REFERENCES

1. Wang B, Peng Y, Yuan F, et al. A comprehensive review of carbons anode for potassium-ion battery: fast kinetic, structure stability and electrochemical. *J Power Sources*. 2021;484:229244.
2. Huang C, Liu Y, Zheng R, et al. Interlayer gap widened TiS_2 for highly efficient sodium-ion storage. *J Mater Sci Technol*. 2022;107:64-69.

3. Zheng R, Yu H, Zhang X, et al. A $TiSe_2$ -graphite dual ion battery: fast Na-ion insertion and excellent stability. *Angew Chemie Int Ed*. 2021;60(34):18430-18437.
4. Li X, Wang Y, Lv L, Zhu G, Qu Q, Zheng H. Electroactive organics as promising anode materials for rechargeable lithium ion and sodium ion batteries. *Energy Mater*. 2022;2(3):200014.
5. Sheng C, Yu F, Li C, et al. Diagnosing the SEI layer in a potassium ion battery using distribution of relaxation time. *J Phys Chem Lett*. 2021;12(8):2064-2071.
6. Zhang L, Chen Y. Electrolyte solvation structure as a stabilization mechanism for electrodes. *Energy Mater*. 2022;1:100004.
7. Huang H, Xu R, Feng Y, et al. Sodium/potassium-ion batteries: boosting the rate capability and cycle life by combining morphology, defect and structure engineering. *Adv Mater*. 2020;32(8):1904320.
8. He H, Zhang H, Huang D, et al. Harnessing plasma-assisted doping engineering to stabilize metallic phase $MoSe_2$ for fast and durable sodium-ion storage. *Adv Mater*. 2022;34(15):e2200397.
9. Tapia-ruiz N, Armstrong AR, Alptekin H, et al. 2021 roadmap for sodium-ion batteries. *J Phys Energy*. 2021;3:031503.
10. Chong S, Qiao S, Wei X, et al. Sb2S3-based conversion-alloying dual mechanism anode for potassium-ion batteries. *iScience*. 2021;24(12):103494.
11. Leite MM, Martins VL, Vichi FM, Torresi RM. Electrochemistry of sodium titanate nanotubes as a negative electrode for sodium-ion batteries. *Electrochim Acta*. 2020;331:135422.
12. Zhang Q, Guo Y, Guo K, Zhai T, Li H. Ultrafine potassium titanate nanowires: a new Ti-based anode for sodium ion batteries. *Chem Commun*. 2016;37:6229-6232.
13. Cech O, Vanýsek P, Chladil L, Castkova K. Mixed Sodium titanate as an anode for sodium-ion battery. *ECS Trans*. 2016;1:331.
14. Zou W, Fan C, Li J. Sodium titanate/carbon (Na_2 Ti_3O_7/C) nanofibers via electrospinning technique as the anode of sodium-ion batteries. *Chinese J Chem*. 2017;1:79-85.
15. Senguttuvan P, Rousse G, Seznec V, Tarascon J-M, Palacín MR. Na_2 Ti_3O_7: lowest voltage ever reported oxide insertion electrode for sodium ion batteries. *Chem Mater*. 2011;18:4109-4111.
16. Han J, Xu M, Niu Y, et al. Exploration of $K_2Ti_8O_{17}$ as an anode material for potassium-ion batteries. *Chem Commun*. 2016;75:11274-11276.
17. Dong S, Li Z, Xing Z, Wu X, Ji X, Zhang X. Novel potassium-ion hybrid capacitor based on an anode of $K_2Ti_6O_{13}$ microscaffolds. *ACS Appl Mater Interfaces*. 2018;18:15542-15547.
18. Griffith KJ, Harada Y, Egusa S, et al. Titanium niobium oxide: from discovery to application in fast-charging lithium-ion batteries. *Chem Mater*. 2021;1:4-18.
19. Yuan T, Soule L, Zhao B, et al. Recent advances in titanium niobium oxide anodes for high-power lithium-ion batteries. *Energy Fuels*. 2020;11:13321-13334.
20. Yang C, Deng S, Lin C, et al. Porous $TiNb_{24}O_{62}$ microspheres as high-performance anode materials for lithium-ion batteries of electric vehicles. *Nanoscale*. 2016;44:18792-18799.
21. Yu H, Cheng X, Zhu H, et al. Deep insights into kinetics and structural evolution of nitrogen-doped carbon coated $TiNb_{24}O_{62}$ nanowires as high-performance lithium container. *Nano Energy*. 2018;54:227-237.
22. Zhu Qi, Jiang J, Li Z, Xu Y, Dou H, Zhang X. Electrospinning oxygen-vacant $TiNb_{24}O_{62}$ nanowires simultaneously boosts electrons and ions transmission capacities toward superior lithium storage. *Electrochim Acta*. 2021;388:138656.
23. Jiang J, Li Z, Nie G, et al. Encapsulating oxygen-deficient $TiNb_{24}O_{62}$ microspheres by N-doped carbon nanolayer boosts capacity and stability of lithium-ion battery. *Batter Supercaps*. 2020;12:1360-1369.
24. Yu H, Lan H, Yan L, et al. $TiNb_2O_7$ hollow nanofiber anode with superior electrochemical performance in rechargeable lithium ion batteries. *Nano Energy*. 2017;38:109-117.
25. Huang Y, Li X, Luo J, et al. Enhancing sodium-ion storage behaviors in $TiNb_2O_7$ by mechanical ball milling. *ACS Appl Mater Interfaces*. 2017;10:8696-8703.
26. Li S, Cao Xi, Schmidt CN, et al. $TiNb_2O_7$/graphene composites as high-rate anode materials for lithium/sodium ion batteries. *J Mater Chem A*. 2016;11:4242.
27. Shang B, Peng Q, Jiao X, Xi G, Hu X. $TiNb_2O_7$/carbon nanotube composites as long cycle life anode for sodium-ion batteries. *Ionics (Kiel)*. 2019;4:1679.
28. Griffith KJ, Seymour ID, Hope MA, et al. Ionic and electronic conduction in $TiNb_2O_7$. *J Am Chem Soc*. 2019;42:16706-16725.
29. Li S, Chen J, Gong X, Wang J, Lee PS. Holey graphene-wrapped porous $TiNb_{24}O_{62}$ microparticles as high-performance intercalation pseudocapacitive anode materials for lithium-ion capacitors. *NPG Asia Mater*. 2018;10:406-416.
30. Zhang Y, Zhang M, Liu Y, et al. Oxygen vacancy regulated $TiNb_2O_7$ compound with enhanced electrochemical performance used as anode material in Li-ion batteries. *Electrochim Acta*. 2020;330:135299.
31. Utetiwabo W, Zhou L, Tufail MK, et al. Insight into the effects of dislocations in nanoscale titanium niobium oxide ($Ti_2Nb_{14}O_{39}$) anode for boosting lithium-ion storage. *J Colloid Interface Sci*. 2022;608:90-102.
32. Yang Y, Li Y, Liu K, et al. Hierarchical porous $TiNb_2O_7$@N-doped carbon microspheres as superior anode materials for lithium ion storage. *Int J Hydrogen Energy*. 2021;5:3425-3436.
33. Deng S, Luo Z, Liu Y, et al. $Ti_2Nb_{10}O_{29-x}$ mesoporous microspheres as promising anode materials for high-performance lithium-ion batteries. *J Power Sources*. 2017;362:250-257.
34. Deng S, Zhu H, Wang G, et al. Boosting fast energy storage by synergistic engineering of carbon and deficiency. *Nat Commun*. 2020;132:1.
35. Yoon S, Lee S-Y, Nguyen TL, Kim IlT, Woo S-G, Cho KY. Controlled synthesis of dual-phase carbon-coated Nb_2O_5/$TiNb_2O_7$ porous spheres and their Li-ion storage properties. *J Alloys Compd*. 2018;731:437-443.
36. Zhu G, Li Q, Che R. Hollow $TiNb_2O_7$@C spheres with superior rate capability and excellent cycle performance as anode material for lithium-ion batteries. *Chem A Eur J*. 2018;49:12932.
37. Hong Bo-J, Hsiao C-W, Bakare F, Sun J-T, Shih S-J. Effect of acetic acid concentration on pore structure for mesoporous bioactive glass during spray pyrolysis. *Materials (Basel)*. 2018;6:963.
38. Yu H, Cheng X, Zhu H, et al. Deep insights into kinetics and structural evolution of nitrogen-doped carbon coated $TiNb_{24}O_{62}$ nanowires as high-performance lithium container. *Nano Energy*. 2018;54:227-237.
39. Griffith KJ, Senyshyn A, Grey CP. Structural stability from crystallographic shear in TiO_2–Nb_2O_5 phases: cation

ordering and lithiation behavior of $TiNb_{24}O_{62}$. *Inorg Chem*. 2017;7:4002-1369.

40. Jiang J, Li Z, Nie G, et al. Encapsulating oxygen-deficient $TiNb_{24}O_{62}$ microspheres by N-doped carbon nanolayer boosts capacity and stability of lithium-ion battery. *Batter Supercaps*. 2020;12:1360-1369.
41. Stobinski L, Lesiak B, Malolepszy A, et al. Graphene oxide and reduced graphene oxide studied by the XRD, TEM and electron spectroscopy methods. *J. Electron Spectros Relat Phenomena*. 2014;195:195-154.
42. Jiao X, Qiu Y, Zhang L, Zhang X. Comparison of the characteristic properties of reduced graphene oxides synthesized from natural graphites with different graphitization degrees. *RSC Adv*. 2017;82:52337.
43. Perumbilavil S, Sankar P, Priya Rose T, Philip R. White light Z-scan measurements of ultrafast optical nonlinearity in reduced graphene oxide nanosheets in the 400–700 nm region. *Appl Phys Lett*. 2015;82:051104.
44. Balaji Mohan V, Liu D, Jayaraman K, Stamm M, Bhattacharyya D. Improvements in electronic structure and properties of graphene derivatives. *Adv Mater Lett*. 2016;82(6):421-429.
45. Dhanalakshmi J, Iyyapushpam S, Nishanthi ST, Malligavathy M, Pathinettam Padiyan D. Investigation of oxygen vacancies in Ce coupled TiO_2 nanocomposites by Raman and PL spectra. *Adv Nat Sci Nanosci Nanotechnol*. 2017;1:015015.
46. Kim S, Jung H, Lim WG, et al. A versatile strategy for achieving fast-charging batteries via interfacial engineering: pseudocapacitive potassium storage without nanostructuring. *Small*. 2022;27:1.
47. Song H, Jeong TG, Moon YH, et al. Stabilization of oxygen-deficient structure for conducting $Li_4Ti_5O_{12-\delta}$ by molybdenum doping in a reducing atmosphere. *Sci Rep*. 2014;4:4350.
48. Song H, Kim Y-T. A Mo-doped $TiNb_2O_7$ anode for lithium-ion batteries with high rate capability due to charge redistribution. *Chem Commun*. 2015;48:9849-9852.
49. Han X, Russo PA, Triolo C, Santangelo S, Goubard-Bretesché N, Pinna N. Comparing the performance of Nb_2O_5 composites with reduced graphene oxide and amorphous carbon in Li- and Na-ion electrochemical storage devices. *ChemElectroChem*. 2020;7:1689-1698.
50. Yan L, Chen G, Sarker S, et al. Ultrafine Nb_2O_5 nanocrystal coating on reduced graphene oxide as anode material for high performance sodium ion battery. *ACS Appl Mater Interfaces*. 2016;7:22213-22219.
51. Xu Y, Memarzadeh Lotfabad E, Wang H, et al. Nanocrystalline anatase TiO_2: a new anode material for rechargeable sodium ion batteries. *Chem Commun*. 2013;79:8973.
52. Hwang J-Y, Du H-L, Yun B-N, et al. Carbon-free TiO_2 microspheres as anode materials for sodium ion batteries. *ACS Energy Lett*. 2019;2:494-501.
53. Patra J, Wu S-C, Leu I-C, et al. Hydrogenated anatase and rutile TiO_2 for sodium-ion battery anodes. *ACS Appl Energy Mater*. 2021;6:5738.
54. Lukatskaya MR, Dunn B, Gogotsi Y. Multidimensional materials and device architectures for future hybrid energy storage. *Nat Commun*. 2016;7:12647.
55. Chang X, Huang T, Yu J, Li J, Wang J, Wei Q. Pseudocapacitive anode materials toward high-power sodium-ion capacitors. *Batter Supercaps*. 2021;10:1567.
56. Van Den Bergh W, Stefik M. Understanding rapid intercalation materials one parameter at a time. *Adv Funct Mater*. 2022;32(31):2204126.
57. Wang W, Kang Z, Sun C-F, Li Y. $K_{2.13}V_{1.52}Ti_{0.48}(PO_4)_3$ as an anode material with a long cycle life for potassium-ion batteries. *Electrochem Commun*. 2022;136:107247.
58. Han J, Niu Y, Bao S-J, Yu Y-N, Lu S-Y, Xu M. Nanocubic $KTi_2(PO_4)_3$ electrodes for potassium-ion batteries. *Chem Commun*. 2016;78:11661-11664.
59. Lee G-W, Park BH, Nazarian-Samani M, Kim YH, Roh KC, Kim K-B. Magnéli phase titanium oxide as a novel anode material for potassium-ion batteries. *ACS Omega*. 2019;3:5304-5309.
60. Kishore B, Gopal V, Munichandraiah N. $K_2Ti_4O_9$: a promising anode material for potassium ion batteries. *J Electrochem Soc*. 2016;163(13):A2551.
61. Han J, Xu M, Niu Y, et al. Exploration of $K_2Ti_8O_{17}$ as an anode material for potassium-ion batteries. *Chem Commun*. 2016;75:11274-11276.
62. Wei Z, Wang D, Li M, et al. Fabrication of hierarchical potassium titanium phosphate spheroids: a host material for sodium-ion and potassium-ion storage. *Adv Energy Mater*. 2018;27:1.
63. Amardeep A, Shende RC, Gandharapu P, Wani MS, Mukhopadhyay A. Faceted antimony particles with interiors reinforced with reduced graphene oxide as high-performance anode material for sodium-ion batteries. *ACS Appl Mater Interfaces*. 2022;40:45296.
64. Brezesinski T, Wang J, Tolbert SH, Dunn B. Ordered mesoporous α-MoO_3 with iso-oriented nanocrystalline walls for thin-film pseudocapacitors. *Nat Mater*. 2010;9:146-151.
65. Augustyn V, Simon P, Dunn B. Pseudocapacitive oxide materials for high-rate electrochemical energy storage. *Energy Environ Sci*. 2014;5:1597.
66. Babu B, Shaijumon MM. Studies on kinetics and diffusion characteristics of lithium ions in $TiNb_2O_7$. *Electrochim Acta*. 2020;345:136208.
67. Ise K, Morimoto S, Harada Y, Takami N. Large lithium storage in highly crystalline $TiNb_2O_7$ nanoparticles synthesized by a hydrothermal method as anodes for lithium-ion batteries. *Solid State Ionics*. 2018;320:7-15.
68. Hummers WS, Offeman RE. Preparation of graphitic oxide. *J Am Chem Soc*. 1958;6:1339-1339.

SUPPORTING INFORMATION

Additional supporting information can be found online in the Supporting Information section at the end of this article.

How to cite this article: Vijaya Kumar Saroja AP, Wang Z, Tinker HR, Wang FR, Shearing PR, Xu Y. Enabling intercalation-type $TiNb_{24}O_{62}$ anode for sodium- and potassium-ion batteries via a synergetic strategy of oxygen vacancy and carbon incorporation. *SusMat*. 2023;1-13. https://doi.org/10.1002/sus2.113